Mathematical and Critical Physics Analysis of Engineering Problems: Old-New Way of Doing Things

Vadim N. Smelyanskiy[1], Veatcheslav V. Osipov and Dmitry G. Luchinsky and Vasyl Hafiychuk
Applied Physics Group, NASA Ames Research Center, MS 269-3, Moffett Field, CA, 94035, USA

In a modern world, importance of computer modeling for solving complex engineering problems cannot be overstated. However, in a number of critical engineering problems computational models cannot provide unique answer and so further physical and analytical insight is required to guide computer simulations. Such an insight becomes even more valuable when off-nominal regimes of operation have to be considered. To deal with complexity of the physical process at the interface of multiple engineering systems a new discipline is emerging – operational physics of critical missions. This discipline combines an old-good physics based approach to modeling engineering problems with modern advanced technologies for analyzing continuous and discrete information flow involving multiple modes of operation in uncertain environments, unknown state variables, heterogeneous software and hardware components. In this paper the new approach is illustrated using as an example analysis of the critical physics phenomena that lead to Challenger accident including physics of cryogenic explosion and propagation of detonation waves, internal ballistics of SRM's in the presence of the case breach fault, and monitoring of the structural integrity of the spacecraft.

Nomenclature

ρ	=	gas density
p	=	gas pressure
T	=	gas temperature
u	=	gas velocity
v_m	=	velocity of metal melting front
v_n	=	velocity of nozzle ablation front
c	=	sound velocity
M	=	Mach number, $M = u/c$
c_V	=	specific heat for constant volume
c_p	=	specific heat for the constant pressure
γ	=	ration of specific heats $\gamma = c_P/c_V$
l	=	perimeter of propellant cross-section

[1]{Vadim.N.Smelyanskiy,Viatcheslav.V.Osipov@nasa.gov,Dmitry.G.Luchinsky,Vasyl.Hafiychuk@nasa.gov}@nasa.gov

e_t	=	total energy of the gas
h_t	=	total enthalpy of the gas
l_h	=	perimeter of hole cross-section
r_n	=	radius of nozzle throat
s_t	=	cross section of the nozzle throat
r_h	=	minimum radius of leak hole
s_h	=	cross-section of hole throat
r_{met}	=	radius of hole in metal case
r_i	=	radius of hole in insulator layer
L	=	length of the propellant grain
L_0	=	typical length equal to 1m
S_b	=	total area of the burning surface
F_N	=	normal thrust
F_h	=	additional thrust produced by hole gas flow
r_b	=	burning rate of solid propellant
n	=	exponent for burning rate of the propellant
ρ_p	=	density of the solid propellant
H_p	=	combustion heat of the solid propellant
Q	=	heat flow from the gas to the walls of the hole
S	=	cross-section of the combustion chamber
f_{tr}	=	surface friction force
T_m	=	melting temperature point
T_a	=	critical temperature of the nozzle ablation
T_c	=	temperature of metal case far from hole
c_m	=	specific heat of case metal
q_{ins}	=	latent heat of insulator ablation
q_m	=	latent heat of metal melting
c_n	=	specific heat of nozzle material
q_n	=	specific heat of ablation of insulator layer
ρ_m	=	density of case metal
ρ_n	=	density of nozzle material
k	=	the thermal conductivity
μ	=	dynamical viscosity of hot gas
Pr	=	the Prandtl number, $Pr=\mu Cp/k$
h	=	subscript for gas parameters in the hole
N	=	subscript for parameters in normal regime
0	=	subscript for stagnation values of gas par
a	=	radius of debond (delamination)
w	=	out of plane displacement
k_{ij}	=	wavenumber i in the medium j
r	=	radius vector from the fault center
J_n	=	the Bessel functions of the first kind
H_n	=	the Hankel functions of the first kind
c_i	=	molar concentration of the i-th component [mole/m^3]
G_{comb}	=	burning rate [mole/sec/m^3]
M_i	=	molar mass of the i-th component [kg]
R_g	=	universal gas constant [J/kg/K]
R_0	=	bubble radius [m]
j	=	mass flux [kg/m^2/sec]
Q_h	=	heat of combustion [J/kg]
q_h	=	heat of evaporation [J/kg]
α_{abs}	=	absorption coefficient
β	=	accommodation coefficient in Eq.(4)

σ	=	surface tension [N/m]

Subscripts

g	=	gas
l,L	=	liquid
v	=	vapor
0	=	initial state
mix	=	mixture
max	=	maximum
ign	=	ignition
evap	=	evaporation

Abbreviation

H2	=	hydrogen
Ox	=	oxygen
N2	=	nitrogen
GH2	=	gaseous hydrogen
LH2	=	liquid hydrogen
GOx	=	gaseous oxygen
LOx	=	liquid oxygen

I. Introduction

IN a modern world, importance of computer modeling for solving complex engineering problems cannot be overstated. In application to Space Exploration, everything, from computational fluid dynamics to microscopic models of material behavior in thermal protection systems and also to guidance, navigation and control, requires complex computer models and software packages that are validated over decades of dedicated studies, comparison with empirical data and theory analysis. Quality and reliability of computer models are often validated through comparison of their outcomes with those of other similar models as an incremental development and through comparison of the model prediction with results of the laboratory and field test studies.

Conceptually, critical physics analysis evolves in the opposite direction. It often begins when observed effects are cannot understand within the scope of existence models, and also when there is an unexplained discrepancy between the computer model predictions and experimental data, when root-causes of system failure need to be understood, when a puzzle emerges from the nontrivial interplay between seemingly distant physics disciplines, when the vehicle performance is studied outside of nominal operational margins or the overly conservative margins and knockdown factors need to be improved. Critical physics analysis plays a major role in situations where substantially different environments, mission durations, operational modes, states and constraints exist that we do not yet understand with our existing experience.

As a very active trend in utilizing the ultra-scale, multi-core high performance computing systems is in incorporating more physics in the algorithms derived from the partial differential equations (PDE) models which allow to better use such systems to tackle previously intractable problems and overcome constrains of massively parallel systems related to power consumption and limitations of single central processing unit (CPU) speeds. Even modern high-end computers may not be sufficient to simulate the complex operational/vehicle environments with enormous variety of temporal and spatial scales in highly nonlinear, multiphase and complex geometry systems. And even when such simulations are possible “in principle” they are not necessarily feasible in terms of resource allocation due to the huge number of required individual analyses and their scopes. Best results can often be achieved by combining simplified physics-based models developed with theoretical methods and critical physics insight that helps to discern, qualify and quantify key phenomena and causality relations within complex environments provided by computer simulations. Best results are achieved through an interdisciplinary effort that combines computer simulations and physics analysis with laboratory and field experiments, mathematical modeling, optimization algorithms and data driven techniques.

This approach is especially important in the era of limited funds, where we must optimize all science, technology and risk reduction investments for development projects. Many problems that we face are integrated in nature, interrelated in solution, and interdependent in application. We should look for a way to prioritize, focus, and “solve

the right problem." There must be a systems approach and it must model the whole physical problem. Therefore all efforts must include a critical "physics based" element in combination with value stream assessment and a system analysis to optimize. Insights gained from fundamental physics investigations can help in technology definition process by reducing risks of selecting among the competing technologies, by providing guidance in the development of these technologies, integration of different technologies into a complete system and choice of cross-cutting, flexible developmental paths.

There exists a deep interrelation between the physics-based approaches and Integrated System Health Management. The objective of critical physics analysis here is to confine the space of designs, level of automation and fault management strategies to obey the set of constraints driven by the operational physics and to inform about possible increase in failures probability due to additional automation tasks and sensor/computer hardware related to them. Development of leading-order physics models is also a necessity in Engineering Risk Assessment to capture the main cause-and-effect sequences and to perform sensitivity studies. This assessment includes dynamic, quantitative models and explicit analysis of the physics-based interactions and mechanisms that drive operational risks and sensor errors.

It follows from this discussion that there is a significant and growing need in development of deep insights and simplified models to capture the nature of complex phenomena in operational-mission environments. At the same time, critical analysis based on fundamental physics investigations still remains a somewhat rare commodity in NASA experience, a "work of art", that is largely lost at NASA since 1960s and 70s. Below we shall demonstrate the development of this approach in a number of recent applications. We shall also discuss the interplay between theory analysis and physics experiment extrapolated from conventional academic-style laboratory setting to a real-world NASA testing realm.

II. Cavitation-induced ignition and explosions of H2/Ox aerosol mixtures

The Challenger disaster of 1986 stimulated investigations of possible catastrophic events related to the use of cryogenic oxygen/hydrogen (H2/Ox) mixtures as fuels. The Challenger accident study showed that the original source of the disaster was freezing of the O-ring in the lower section of one of the solid boosters and formation of a gas leak through the O-ring [1,2]. This leak developed into a strong jet of the liquid hydrogen (LH2) from the booster and caused the separation of the lower dome from the rest of LH2 tank (Figure 1, first failure). As a result, the tank began to accelerate upwards under the gas pressure inside the tank. The accelerating LH2 tank broke the liquid oxygen (LOx) feed line in the intertank section between the liquid hydrogen (LH2) and oxygen (LOx) tanks and also the LH2 tank's top dome. The resulting LOx stream from the broken LOx feed line was injected into the intertank space, mixing with the gaseous hydrogen (GH2) jet from the rupture of the LH2 tank top dome and then self-ignited near the intertank section.

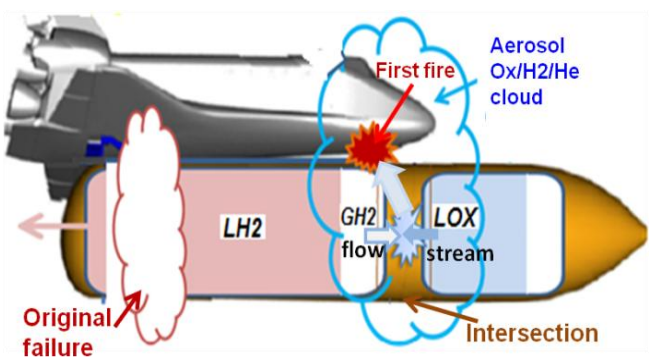

Figure 1. Initiation of the first flash near the Challenger's Orbiter/External tank forward attachment

Importantly, the first fireballs, which caused disintegration of the Orbiter were observed in the areas near the ruptured intertank section between the tank and Challenger surfaces (Fig.1) but not near the hot plume injected from SRB nozzle. The physical mechanism of the self-ignition of cryogenic GH2/LOx mixtures in these areas remains a puzzle despite numerous studies on the subject. Moreover, the explosions in hydrogen-oxygen vertical impact (HOVI) tests performed in White Sands Test Facility (WSTF) at seemingly similar initial mixture conditions varied significantly—from a slow combustion type to a devastating explosion wave with overpressure from tens to hundred atmospheres and velocity many times greater than the sound speed3. Understanding of these phenomena is very important for the proper assessment of risks associated with accidental formation of "super cold" cryogenic mixtures

in vehicle environments. At the same time all existed numerical programs cannot to be able to describe the effect of the self-ignition and combustion of cryogenic aerosol H2/Ox mixtures formed by breach of liquid rocket fuel tanks.

Purposeful experiments with Ox and H2 tanks, HOVI tests and other available empirical data showed that cryogenic H2/Ox mixtures always self-ignite without any external sources when the gaseous hydrogen (GH2) and oxygen (GOx) mix with a LOx stream3. We propose a cavitation-induced self-ignition mechanism of cryogenic H2/Ox fluids. Cavitation is the formation and compression of vapor bubbles in liquids under the action of a pressure jump between the liquid and the gas phases. Due to the inertial motion of the liquid this process leads to a rapid collapse of the bubbles and spiking of the gas temperature and pressure inside, producing strong shock waves4,5 . Here, we discuss some possible scenarios of cavitation-induced ignition in cryogenic Ox/H2 fluids related to the collapse of a vapor bubble in the Ox liquid near the interface between LOx and the GH2/GOx mixture.

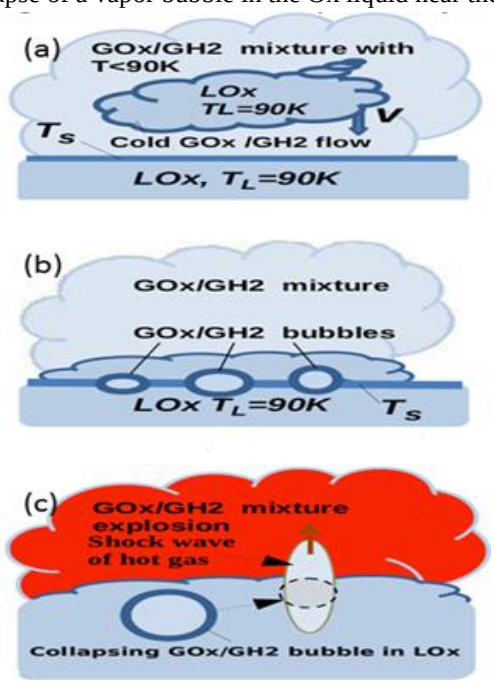

Figure 2. One scenario of cavitation-induced ignition of aerosol H2/Ox mixture: (a) Cooling of surface of LOx pieces by cold GH2; (b) Formation of bubbles with thin cooled liquid layers; (c) Collapse of the bubble, injection of hot gas, and generation of the shock wave by the bubble collapsing near the liquid-mixture interface.

We concentrate on the most transparent scenario of the cavitation-induced ignition that explains the appearance of the fireballs near the intertank section in Challenger accident. Damage of this section results in breaches of the liquid oxygen (LOx) feed line and the LH2 tank's top. The LOx pieces will be ejected from the broken LOx feed line into the intertank space where their surfaces will be cooled by the very cold H2/He gas injected from the rupture of the LH2 tank top dome. One of such pieces flies out from the intersection and impacts on the Challenger surface. Then other LOx piece impacts on the first (Figure 2a). As a result several Ox vapor bubbles with admixed GH2 and cold surface can arise near the interface between of these two LOx pieces (Figure 2b). Pressure of saturated Ox vapor p_s sharply drops with decrease of the liquid-vapor interface temperature: $p_s(T_s) = p_c\left(T_s / T_c\right)^{\lambda}$ where λ=7 (see Ref. 6), p_c=50.43atm and T_c=154.58K are critical pressure and temperature for Ox. For example, p_s=0.12atm at T_s=65K.

Condensation is very intensive process. Therefore, at first the pressure inside of a bubble with cold surface very quickly drops to $p_s(Ts)$, but the pressure in the liquid remains equal to p_{atm}=1atm. The bubble under the action of pressure different ($p_{atm} - p_s$) starts rapidly compression and due to the inertial motion of the liquid this process leads to a sharp periodic collapsing of the bubbles and spiking of the gas temperature and pressure inside the bubble (Figure 3). The presence in the bubble of even a small amount of noncondensable GH2 sharply increases the values of p_{max} and T_{max} due to local explosion of the GH2/GOx mixture. Our simulations show that a bubble of initial radius ~1mm with the surface temperature Ts<70K can compress to size R_{min}~0.1mm and the gas temperature and pressure in such bubble can exceed 2500atm and 1700K, respectively (Figure 3).

Other scenarios of cavitation-induced ignition is considered in Ref. 7 where the pressure jump between LOx and the bubbles assume to arise due to a "weak" shock waves arising as a result of an impact of a LOx piece against a solid object, e.g. a tank wall. Such a shock wave cannot induce ignition of the GH2/GOx mixture directly, but it can initiate cavitation collapse of the vapor bubbles inside LOx. The computations showed that such weak shock waves can lead to the formation of bubbles of a small radius $R_{min} \simeq 0.1$ mm with huge pressures p>1000atm and temperatures T > 2500K inside the bubble (Ref. 7).

The equations analogues those used in the cavitation simulations (see below) were employed to analyze the cavitation-induced ignition of GH2/GOx mixtures by a localized strong shock wave of hot gas generated by the collapsing bubble near the liquid-mixture interface (Figure 2c).

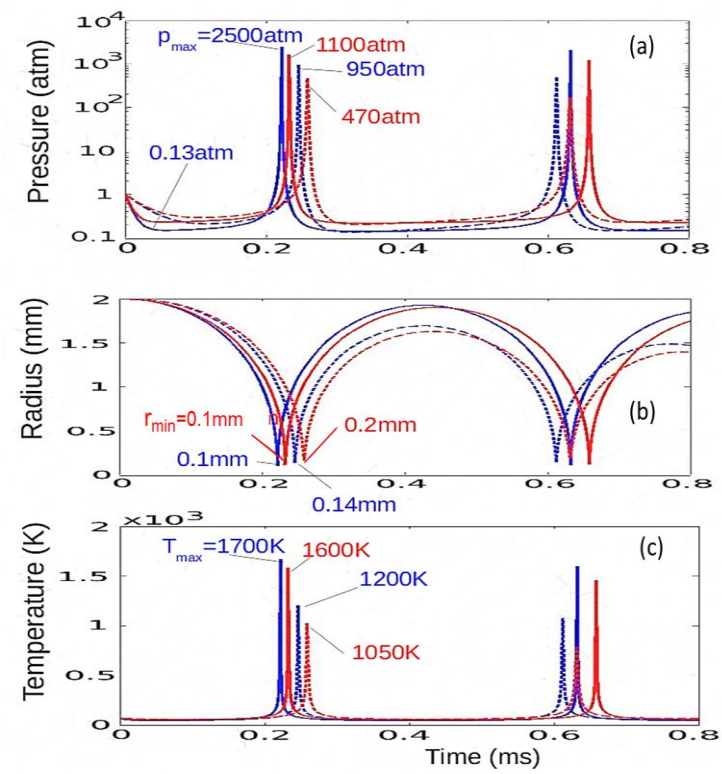

Figure 3. Dynamics of a bubble with cool surface: (a) pressure of H2/Ox mixture inside the collapsing bubbles; (b) bubble radius; (c) gas temperature. Initial conditions: pressure p=1atm inside and outside the bubble and pH2= 0.01atm inside the bubble, surface temperature -Ts= 65K (blue) and 70K (red). Evaporation reflection factor α=1 (solid) and 0.3 (dashed).

We envision a hemispherical shock wave propagating in the unconfined GH2/GOx mixture above the LOx-gas interface (see Fig.1c), initiated by a local increase in gas pressure and temperature within the radius R_{min}. We made sure that the local jump of the pressure p= 200 atm and temperature T=500K in area of radius r_0 = 0.1mm (collapsed bubble) is sufficient to induce ignition and combustion of GH2/GOx/N2 mixtures and even detonation in stoichiometric GH2/GOx mixtures (Figure 4).

We note that in reality the superhot and super-compressed O, H, and OH species forming in the process of GH2/GOx combustion[8,9] inside the bubble may be ejected into the space above the LOx surface and easily ignite the GH2/GOx mixture nearby (Figure 1c).

A. Model for cavitation-induced self-ignition of cryogenic H2/Ox mixtures

To simulation the above novel effects we developed a high-fidelity model of collapsing of Ox vapor bubbles with admixed GH2 taking into consideration the burning inside the bubble. Treating the liquid as incompressible, the equations for the liquid phase (r > R(t)) may be reduced to the equation for the bubble radius R (Ref. 7):

$$R\frac{d^2R}{dt^2}+\frac{3}{2}\left(\frac{dR}{dt}\right)^2+\frac{j_{cd}}{\rho_L}\frac{dR}{dt}+\frac{R}{\rho_L}\frac{dj_{cd}}{dt}=\frac{p_m-p_L}{\rho_L}-\frac{2\sigma}{R\rho_L}+\frac{j_{cd}^2\left(2\rho_L-\rho_m\right)}{2\rho_L^2\rho_m}-\frac{4\mu}{R\rho_L}\left(\dot{R}-\frac{j_{cd}}{\rho_L}\right) \tag{1}$$

and the advection-diffusion equation for the liquid temperature T_l:

$$\frac{\partial T_l}{\partial t}+\left(\frac{R}{r}\right)^2\left(\frac{dR}{dt}+\frac{j_{cd}}{\rho_L}\right)\frac{\partial T_l}{\partial r}=\frac{\kappa_L}{C_L\rho_L r^2}\frac{\partial}{\partial r}\left(r^2\frac{\partial T_l}{\partial r}\right) \tag{2}$$

with initial and boundary conditions:

$$R(t=0)=R_0,\dot{R}(t=0)=0,T_l(0)=T_m(0)=T_L,T_l(r\to\infty)=T_L,T_l(r=R)=T_m(r=R)=T_s. \tag{3}$$

Here r is the radial coordinate, ρ_L = const, C_L and ρ_L are the liquid density, specific heat and thermal conductivity, respectively, p_m and ρ_m are the pressure and the gas mass density, respectively, in the gas mixture at the liquid-gas interface, p_L is the liquid pressure far from the bubble. The Ox vapor condensation flux j_{cd} is given by the well-known Hertz-Knudsen equation:

$$j_{cd} = \frac{\beta\left(p_{Ox} - p_s\left(T_s\right)\right)}{\sqrt{2\pi R_{Ox} T_s}},\ p_s\left(T_s\right) = p_c\left(\frac{T_s}{T_c}\right)^{\lambda} \tag{4}$$

at the liquid-gas interface, R_{Ox} is Ox vapor constant, β is the accommodation coefficient[4,5]. We assume that the equations of state of the gases are:

$$\begin{aligned} p_{H2} &= c_{H2} R_0 T_m, \\ p_{O2} &= c_{O2} R_0 T_m, \\ p_{H2O} &= c_{H2O} R_0 T_m, \\ p_m &= R_0 T_m \sum_i c_i = R_0 T_m c_m \end{aligned} \tag{5}$$

Here R_0, c_i, are the gas constant and mole concentration i - gas, respectively. The total density ρ_m, velocity u_m, temperature T_m and energy E of the mixture are given by:

$$\begin{aligned} &\frac{\partial u_m}{\partial t} + u_m \frac{\partial u_m}{\partial r} = -\frac{R_0}{\rho_m}\frac{\partial T_m c_m}{\partial r}, \\ &\frac{\partial E}{\partial t} + \frac{1}{r^2}\frac{\partial}{\partial r}\left(r^2 u_m\left(p_m + E\right)\right) = \frac{1}{r^2}\frac{\partial}{\partial r}\left(r^2 \kappa_m \frac{\partial T_m}{\partial r}\right) + Q_h G_{comb} \\ &E = \frac{5}{2} R_0 T_m c_m + \frac{1}{2}\rho_m u_m^2,\ \rho_i = c_i M_i,\ \rho_m = \sum_i c_i M_i \end{aligned} \tag{6}$$

Here $\kappa_m = \left(T_m / T_0\right)^{1/2} \sum c_i \kappa_i(T_0) / c_m$ the thermal conductivity of the gas mixture as a function of T_m, Q_m is the combustion heat, and G_{comb} is the combustion rate. The burning of GOx/GH2 mixture is described by 20 chain chemical reactions (see CANTERA CODE in Ref. 10) that include generation of O, H, OH species. For simplicity here we consider a simplified model of the burning that takes into account only main gas components that can arise in a collapsing bubble (at 0 < r < R): oxygen vapor, non-condensable gaseous hydrogen and water generated as a result of the burning. The simplified model based on the assumption that the burning rate is limited by the initiation reactions $H_2+O_2 \rightarrow OH+OH$ and $H_2+O_2 \rightarrow HO_2+H$, which have the lowest rates. Thus, we modeled the GH2/GOx combustion by a brutto reaction $H_2+O_2 \rightarrow H_2O+ 1/2O_2$ with the rate[10,11]

$G_{comb} = c_{H2} c_{Ox}[1.1\cdot 10^8 \exp(-19680/T) + 1.48\cdot T^{2.433}\exp(-26926/T)]m^3/mol/\mathrm{s}$ (T is in degrees Kelvin). We note that this approximation is close to the one-step mechanism of Mitani and Williams[12]. Also, the model predicts the same steady detonation wave parameters as those obtained[3] with the help of the full model describing all main chain reactions of GOx/GH2 mixture combustion[10,12].

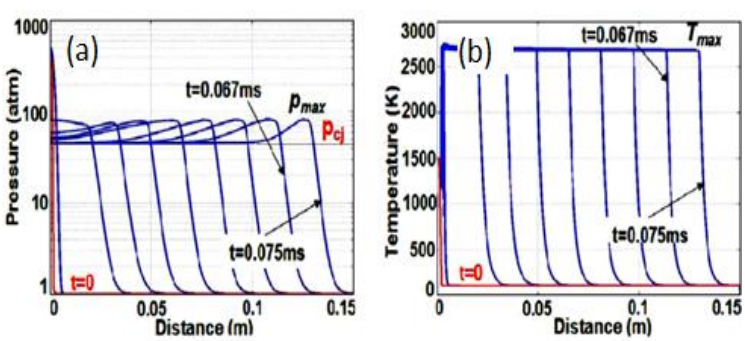

Figure 4. Formation of cavitation-induced hemispheric detonation wave in stoichiometric GH2/GOx mixture

We showed that the dynamics of the gas mixture inside a bubble, taking into account the combustion and high diffusivity

of the light GH2 molecules, can be written as

$$\frac{\partial c_{Ox}}{\partial t}+\frac{1}{r^2}\frac{\partial}{\partial r}(r^2 c_{Ox}u_m)=-\frac{1}{2}G_{comb},\ \frac{\partial c_{H2O}}{\partial t}+\frac{1}{r^2}\frac{\partial}{\partial r}(r^2 c_{H2O}u_m)=G_{comb},$$
$$\frac{\partial c_{H2}}{\partial t}+\frac{1}{r^2}\frac{\partial}{\partial r}(r^2 c_{H2}u_m)+G_{comb}=\frac{1}{r^2}\frac{\partial}{\partial r}\left[r^2 D_{H2}\left(\frac{\partial c_{H2}}{\partial r}-\frac{c_{H2}}{2T_m}\frac{\partial T_m}{\partial r}\right)\right] \tag{7}$$

where $D_{H2}=\left(T_m/T_0\right)^{3/2}\left(p_0/p_m\right)D_{H2}(T_0,p_0)$ is hydrogen diffusion coefficient[12]. Finally, the initial and boundary conditions for above equations are:

$$\frac{\partial T_m}{\partial r}\Big|_{r=0}=0,\left(\kappa_m\frac{\partial T_m}{\partial r}-\kappa_l\frac{\partial T_l}{\partial r}\right)\Big|_{r=R}=j_{cd}q_h,\ \frac{\partial c_i}{\partial r}\Big|_{r=0}=0,\ c_i\big|_{r=0}=c_i^0,\ u_m\big|_{r=0}=0,$$
$$u_m\big|_{r=R}=\frac{\partial R}{\partial t}-\frac{j_{cd}}{c_{Ox}M_{Ox}},\ u_m\big|_{t=0}=0,\ \frac{j_{cd}c_{H2}}{c_{Ox}M_{Ox}}=D_{H2}\left(\frac{\partial c_{H2}}{\partial r}-\frac{c_{H2}}{2T_m}\frac{\partial T_m}{\partial r}\right)\Big|_{r=R}, \tag{8}$$

where q_h is the latent heat of *LOx* vaporization. Additional conditions are presented in Figure 3. The simulations were done using Godunov's scheme with variable time-step for stiff problem. The time step was varied depending on the maximum of the time derivatives of bubble radius, temperature and pressure. In particular we use Monotone Upstream-centered Schemes for Conservation Laws (MUSCL) based numerical scheme that extends the Godunov's scheme idea of linear piecewise approximation to each cell by using slope limited 5 left and right extrapolated states. For simulation (Figure 3 and Figure 4) we used the standard material parameters for hydrogen and oxygen.

III. Explosions of aerosol cryogenic H2/Ox/N2 mixtures

We analyzed HOVI tests in detail and have showed3 that existed experimental investigations[13-16] and theory of deflagration and detonation of cryogenic H2/Ox/N2 mixture8[,9,17-20] cannot explain the HOVI test data (pressure of a few atmospheres, and front velocity of about 600 m/sec that is much less than the detonation velocity and is much higher than the deflagration velocity). Our theoretical analysis of HOVI tests required the development of diverse yet interconnected physics models, from the mechanical model of rapture of fuel tanks, shock formation at ground impact and liquids escaping from the tanks, to flow fragmentation and Leidenfrost effect for the cryogen droplets evaporation at the contact with the hot ground being slowed by film boiling. Size of the H2 and Ox clouds and their mixing before the ignition determined the explosion strength and required calculation of the droplet cloud trajectory in the air and ignition delay in the complex multiphase mixture of fragmented oxygen and hydrogen flows. It is almost impossible to study correctly via computer modeling all such processes that includes dynamics of fuel tank rupture, release liquid and gaseous H2 and Ox fluxes from the ruptured tanks, their evaporation, formation of aerosol clouds and the self-ignition during a short time (~0.1sec) of turbulent intensive mixture of these fluxes. All these extremely complex physics processes can be analyzed based on simplified physics models that allow us to give estimations of the main parameters of those processes that are the most important for ascertainment of general picture of the incident. Physics of liquid droplet combustion is also important for understanding of combustion instabilities and their damping in stage combustion engines.

B. Formation and explosion of aerosol cryogenic H_2/Ox mixtures

The impact of the H2 and Ox tanks can result in the rupture of the bottom domes in both the LH2 and the LOx tank. The turbulent LH2 jet from the breach impinges on the hot ground and breaks into droplets. The rupture of the bottom dome of the LO2 tank for the ground tests occurs with a delay time t_{delay} ~ *20-40msec*. The escaping LO2 stream breaks into droplets that scatter from the tank surface during the time of *~60 msec*. Fragmentation of a liquid stream into droplets is a complex and poorly understood phenomenon. Droplet sizes may vary significantly. The typical droplet radius depends on the parameters of both the liquid and gas[21]. Recent experimental studies of liquid jets impinging on a flat smooth surface established the following empirical correlation for the mean droplet radius[22]:

$$r_d = 2.53\times10^5 d_h \,\mathrm{Re}^{-1.28} We^{0.4} \left(\mu_{LH2}/\mu_{air}\right)^{-1.16}, \mathrm{Re} = \frac{d_h v \rho_L}{\mu_{LH2}}, \mathrm{We} = \frac{d_h v^2 \rho_L}{\sigma_{LH2}}, \tag{9}$$

Here μ is the dynamic viscosity equals to $\mu_{air} = 1.63\times10^{-5}\,Pa\sec$ for air, $\mu_{LH2} = 1.32\times10^{-5}\,Pa\sec$ for LH2, and $\mu_{LO2} = 1.96\times10^{-4}\,Pa\sec$ for LO2, v is liquid velocity, ρ_L is the liquid density, d_h is the stream (hole) diameter, and σ is the surface tension. The velocity in the HOVI tests was $v=v_0=30m/sec$, it was found that the typical radius of the droplets in the H2 cloud is about $r_{dr,H2}$= 8mm and in the Ox cloud is about $r_{dr,O2}$= 0.5 mm. These values are almost independent of the diameter d_h of breach of tank wall.

C. Formation of the aerosol H_2/Ox clouds

The typical droplets of radius r_{dr} and mass $m=4\pi\rho_L r_{dr}^3/3$ bouncing off the ground move with initial velocity of

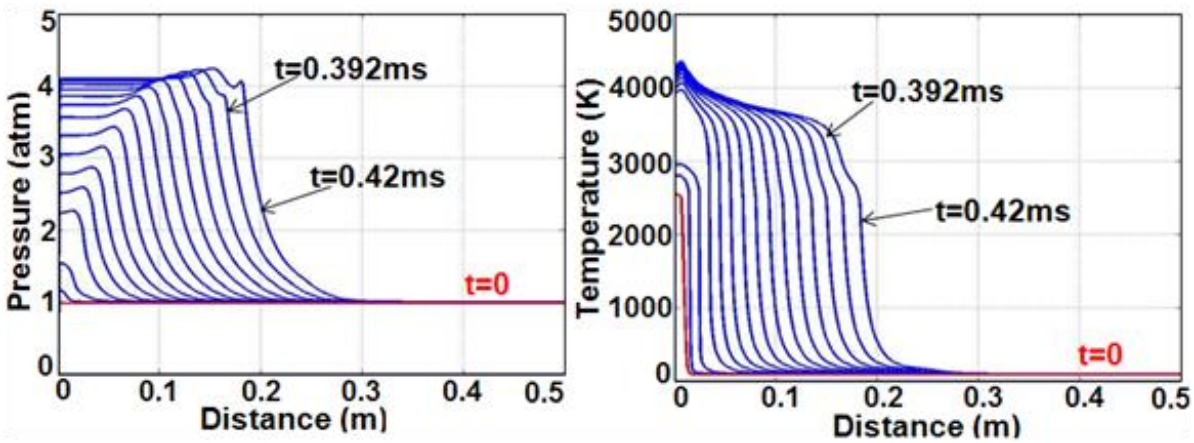

Figure 5. The distributions of pressure and temperature during aerosol combustion in the GH2/GOx/N2 mixture (2:1:4). The combustion wave parameters are p_{max}≅4.2atm, T_{max}=3300K, v=600m/s

order v_0 and fly through the air with temperature T_{air} ≈ 300K and pressure p_{air}= 1atm. The droplet velocity v is slowed by the air drag. The travel distance as functions of time t is equal to:

$$L_v(t) = v_0\tau_v \ln\left(1+\frac{t}{\tau_v}\right), \quad \tau_v \approx \frac{8\rho_L r_{dr}}{1.2\rho_{air} v_0}. \tag{10}$$

It follows from Eq. (10) that the travel distance for HOVI tests is equal to L_v≈ 2.7m for the typical LH2 droplets and the explosion delay time t ≈90msec, and L_v ≈ 2.8m for the typical LOx droplets for the explosion delay time t ≈60msec. These values agree with the observed sizes of the H2 and Ox aerosol clouds. We discussed difference data for HOVI tests with distinct tank volumes and rupture devices and estimated of the escaped H2 and Ox masses before the explosion3.

D. Aerosol explosion and the interpretation of the HOVI data

The aerosol clouds are mixtures of gaseous H2 and Ox and the liquid droplets. HOVI tests showed that the H2 and Ox clouds partly mix during time τ_d ≈*100msec*, and the gaseous H2 and Ox mixture ignites. The temperature of this burning mixture can be about T_{flame}=*3000K÷3900K*. As a result of the combustion of the GH2 and GOx the droplets are evaporated by the contact with the hot combustion products and air. Our estimations showed that main mechanism of evaporation of such lager droplets is IR radiation of the hot gas3. This mechanism is more efficient in the case of the cryogenic aerosols with low critical temperature (T_c=33.2K for H2 and T_c =154.6K for Ox). Under action of the radiation the droplet is rapidly heated almost homogeneously to T_c. The evaporation time for a droplet subject to radiation heat transfer and can be estimated via the following heat balance as,

$$t_{evap} = \tau_{evap}\left(\frac{T_1}{T_{flame}}\right)^4, \qquad \tau_{evap} = \frac{C_L \rho_L \left(T_c - T_L\right) r_{dr}}{3\eta^* \sigma T_0^4} \tag{11}$$

where σ=5.67x10^{-8}W/m^2/K^4 is the Stephan-Boltzmann constant, T_1=3500K is the characteristic flame temperature. and η is the absorption efficiency, $\eta = 0.1 \div 05$ according to the infrared absorption data in[23,24,25]. The evaporation time strongly depends on the flame temperature T_{flame}. The vaporization of the LH2 and LOx droplets results in an abrupt increase of the combustible gas density and leads to a strong buildup of pressure in the combustion products. To simulate aerosol combustion, Eqs. (5) - (8) were used and in Eqs. (7) the terms $\left(c_{H2,Ox}^{drop} / \tau_{evap}\right)\left(T_g / T_1\right)^4$ are added where c_{H2}^{drop} and c_{Ox}^{drop} are molar density of droplets of LH2 and LOx. We note that these terms characterizing generation of gaseous explosive H2/Ox mixture is proportional to $\left(c_{H2,Ox}^{drop} / \tau_{evap}\right)$. It means that the inaccurate estimation of τ_{evap} can be corrected by relevant fitting of $c_{H2,Ox}^{drop}$ value. Fitting of the value of $\left(c_{H2,Ox}^{drop} / \tau_{evap}\right)$ we showed that the observed HOVI test data can be successfully explained based on aerosol combustion. For example, combustion of aerosols with $C_{H2}^{droplet} = 20 mol/m^3$ $(\rho_{H2}^{droplet} = 0.04 kg/m^3)$ and $C_{Ox}^{droplet} \approx 10 mol/m^3$ $(\rho_{ox}^{droplet} \approx 0.32 kg/m^3)$ and

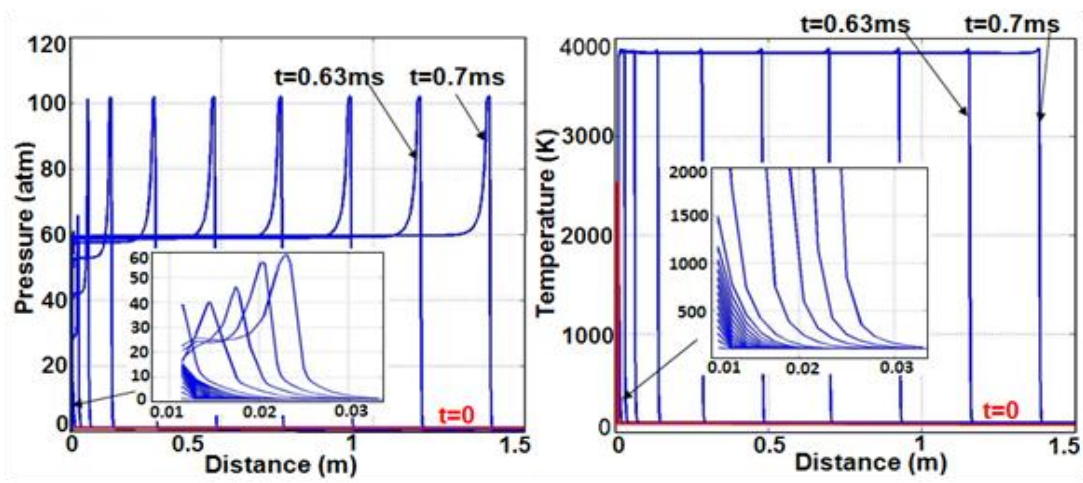

Figure 6. Formation of detonation wave in an aerosol H2/O2 mixture (2:1). The inserts show early stages of the processes.

the evaporation time $\tau_{evap} = 1ms$ allows us to explain the typical sensor HOVI data for an explosion wave with p_{max}≈*4atm* and front velocity *v≈600m/sec* (see Figure 5 and Figure 6).

Our analysis revealed important result: only a small fraction of the escaped cryogen mass participates in formation of the strong explosion wave, main part of aerosol H2/Ox clouds is burned down slowly. This result leads to an important conclusion: a strong detonation explosion can be initiated by a spark or a hot object in an extensive aerosol mixture, not just by a strong shock wave, as is the case for cryogenic gaseous mixtures. Note also that the maximum pressure of the aerosol detonation wave can exceed that of the detonation wave in the gas mixtures. The aerosol detonation scenario was apparently realized in one of the HOVI tests when well mixed dense aerosol H2 and Ox clouds was formed before the ignition of these mixture.

IV. Integrated System Health Management for Solid Rocket Motors

As was explained in the beginning of the previous section the root cause of the Challenger accident was the case was breached1[,2,26] of the SRM. It is clear in this context that the development and deployment of an integrated system health management (ISHM) approach for the SRMs is a prerequisite for the safe exploration of space with the next-generation of Crew Launch Vehicles and an essential part of the novel safety strategy adopted by NASA. In

this section we discuss a physics-based approach to the solution of this problem, including in particular an analysis of the case breach fault.

At the core of an on-board ISHM approach for SRMs are the real-time failure detection and prognostics (FD&P) technique. Several facts render the SRMs unique for the purposes of FD&P: (i) internal hydrodynamics of SRMs is nonlinear, (ii) there is a number of failure modes that may lead to abrupt changes of SRMs parameters, (iii) the number and type of sensors available on-board are severely limited; (iv) the only available recovery resource being a limited thrust vector control authority; (v) the safe time window between the detectable onset of a fault and a possible catastrophic failure is typically a few seconds. The overarching goal of SRM FD&P is to extract information from available data with precise timing and a highest reliability. In order to enable in-flight FD&P we are developing physics-based forward models of the on- and off-nominal SRM operation and Bayesian sensor-fusion framework for tracking the state and parameters of the SRM.

A. Internal ballistics of the SRM

The internal ballistics of the SRMs in the presence of the fault can be conveniently described by the following set of stochastic partial differential equations representing conservation laws for mass momentum, and energy of the gas[27,27-33]

$$\partial_t \left(UA_p \right) + \partial_x \left(f(U) A_p \right) = S, \tag{12}$$

where conservative variables of the gas dynamics and function $f(U)$ are given by the following equations

$$U = \begin{bmatrix} \rho \\ \rho u \\ \rho e_T \end{bmatrix}, \quad f(U) = \begin{bmatrix} \rho u \\ \rho u^2 + p \\ \rho u e_T + up \end{bmatrix}, \tag{13}$$

$e_t = c_V T + I^2/2$, $h_t = c_p T + u^2/2$, are the total energy and total enthalpy of the gas flow, $H = c_0 T_0$ is the combustion heat of solid propellant and the source terms that include fault terms at a given location x_0 have the form

$$S = \begin{bmatrix} \rho_p \dot{R} l(x) - \rho_{t,h} u_{t,h} A_h \delta(x - x_0) \\ p \partial_x A_p - \lambda \rho u^2 l(x) \\ H \rho_p \dot{R} l(x) - h_{t,h} \rho_{t,h} u_{t,h} A_h \delta(x - x_0) \end{bmatrix}. \tag{14}$$

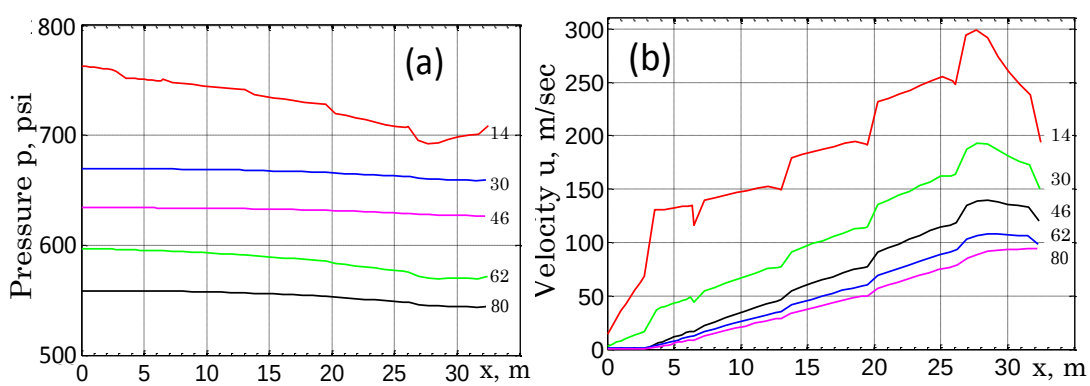

Figure 7. Nominal regime: Results of numerical solution of Eqs. (15), (16) for axial distributions of pressure (a) and velocity (b) at different moments of time. Time after ignition: 14, 30, 46, 62, and 80 seconds. The value of x is measured from the motor head.

This model extends the previous work[27,27] in a number of important directions. To model various uncontrollable sources of noise (such as cracks and case vibrations) that may become essential in off-nominal conditions and may screen the variation of the system parameters a random component in the propellant density $\rho p \to \rho p[1+\sqrt{\sigma}\cdot\xi(t)]$ is introduced. Various faults can be modeled within the set of Eqs. (12) -(14) (including nozzle failure, propellant cracking, bore choking, and case breach) by choosing the time scale and direction of the geometrical alternations of the grain and case and the corresponding form of the source/sink terms. In particular, for the case breach fault two additional terms in the 1st and 3rd equations in Eqs. (14) correspond to the mass and energy flow from the combustion chamber through the hole in the rocket case with cross-section area A_h(t).

Combining the equations of gas dynamics with the dynamics of propellant regression, nozzle ablation, and case breach fault the performance model of the large segmented SRM in the presence of faults can be summarized[29-33] in the set of Eqs. (15) with the conservative variables U and function $f(U)$ given by Eq. (13) and the source terms S given by Eq. (14).

$$\begin{cases} \partial_t\left(UA_p\right)+\partial_x\left(f(U)A_p\right)=S, \\ A_p(x_i)=f_{Ai}(R(x_i)), \qquad l(x_i)=f_{li}(R(x_i)), \\ \dot{R}=ap^n+C\left(I-I_{cr}\right), \\ \dot{R}_t=v_{m,t}\left(\dfrac{p_0}{p_{\max}}\right)^{1-\beta}\left(\dfrac{R_t}{R_{t,in}}\right)^{-\beta}, \\ \dot{R}_{ex}=v_{m,ex}\left(\dfrac{p_0A_t}{p_{\max}A_{ex,in}}\right)^{1-\beta}\left(\dfrac{R_{ex}}{R_{ex,in}}\right)^{-\beta}\dfrac{\left(T_{ex}-T_{abl}\right)}{\left(T_t-T_{abl}\right)}, \\ \dot{R}_h=\dfrac{Q_c+Q_R+Q_b}{\left[q_{met}+C_{met}\left(T_{mel}-T_{m0}\right)\right]\rho_{met}}. \end{cases} \tag{15}$$

Here $R(t)$, R_t(t), R_e(t) , and Rh(t) are radiuses of the burning surface, nozzle throat, nozzle exit, and of the case breach fault (hole in the metal case) respectively. To model the actual propellant geometry along the rocket axis the combustion chamber is divided into N segments[31]. For each ballistic element i[th] the port area $A_p(x_i)$ and perimeter $l(x_i)$ averaged over the segment length dx_i are provided in the form of the design curves $A_p(x_i)=f_{Ai}(R(x_i))$ and $l(x_i)=f_{li}(R(x_i))$.

The heat flow terms due to radiation QR, convection Qc, and burning of the metal surface in the hot gas flow through the hole are given[29-32] by the following relations

$$Q_R=\sigma\left[1-\exp\left(-\lambda p_{t,h}\right)\right]\left(T_t^4-T_{met}^4\right),\quad Q_c=0.023C_p\left(\frac{\gamma p_{t,h}}{\Gamma c_0}\right)^{0.8}\left(\frac{2R_h}{\mu}\right)^{-0.2}\left(T_t-T_{met}\right),\quad Q_b=v_{fb}\left[q_{met}+C_{met}\left(T_{mel}-T_{m0}\right)\right]\rho_m. \tag{16}$$

To model internal ballistics of the SRM the system of equations (15), (16) is integrated forward in time. The important advantage of this model is the ability to reproduce accurately the nominal regime of the quasi-steady burning of the SRM and at the same time to model dynamics of various faults including e.g. nozzle blocking, bare chocking, propellant clacking, and case breach. Another important advantage of the low-dimensional model (15), (16) is that it provides a possibility of a fast on-line inference parameters of the SRM faults. We now verify the model and illustrate its application to the FD&P of the case breach fault.

B. Forward modeling

To integrate model (15), (16) forward in time in quasi-steady regime one can use Euler approximation on a coarse-grained (in general non-uniform) lattice of axial coordinates. The boundary conditions[28] at the aft end (at the outlet of the grain) are defined by the chocking (sonic) conditions at the nozzle throat. The boundary conditions at

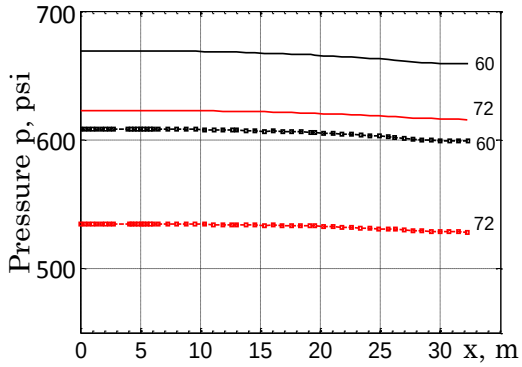

Figure 8 Comparison between spatial distribution of pressure in the nominal regime (solid lines) and off-nominal regime (squares). (right). The time instants from the top to the bottom in the figure are 60 s and 76 s. The time resolution of the calculations was 0.2 s, initial radius of the hole R_{h0} = 0.1 in, burning rate of the hole wall v_m = 0.3 in/s, initial time of the fault 20 s, the fault is located in the middle section.

the rocket head are determined by the continuity conditions of the gas flow from the propellant surface and through the port area at the rocket head.

The results of the numerical solution of the problem (15), (16) pressure (p) and velocity (u) in the nominal regime are presented in Figure 7 for five instances of time with the time step 16 sec (the time resolution of the solution was 0.2sec). It can be seen from the figure that there is a substantial difference between the head and aft pressure and velocity due to the effect of mass addition. An analysis shows that the results presented in the figure coincide with those obtained by the 3rd party using high-fidelity simulation of the internal ballistics of SRM and therefore provide a verification of the low-fidelity model.

C. Modeling case breach fault

To model case breach fault in a large segmented SRM first we have to introduce a parameterization of the fault. It can be shown[29-33] that the fault dynamics is described entirely by the dynamics of the area of the hole $A_h(t)$. The actual dynamics of the fault area can be complicated[34] due to e.g. cracks and nontrivial geometry of the joins. It is therefore convenient to introduce general polynomial parameterization in the form:

$$A_h(t) = a_1 + a_2 t + a_3 t^2 + a_4 t^3. \tag{17}$$

The hole is most likely to be localized at one of the section joints. As a rule, only pressure sensor is available situated in the rocket head. Therefore, we have to verify that the measurements of the head pressure can be used to infer pressure at an arbitrary location of the hole along the rocket axis. To do so we simulate the model of internal ballistics of the SRM in the off-nominal regime with the case breach area dynamics given by (17) at arbitrary location. The results of such simulations for the case breach at the middle of the SRM are shown in the Figure 8. It can be seen from the figure that the pressure drop induced by the case breach is uniform along the rocket axis. and does not depend on the location of the burning-through hole in the case. This result paves a way to a fast on-line estimation of the parameters of the case breach fault.

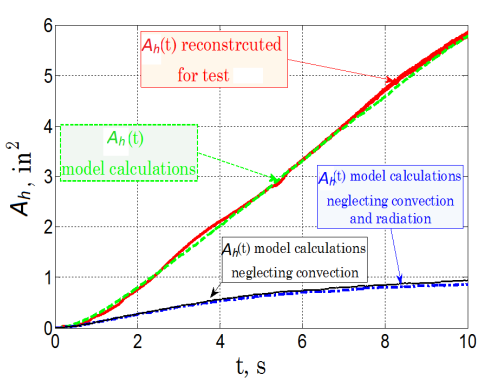

Figure 9 Modeling fault dynamics. The hole area $A_h(t)$ reconstructed from the test data are shown by red lines. The results of the fit using Eqs (15), (16) are shown by green dashed lines. The results of the same calculations, but neglecting term Q_b (black solid line)/; neglecting both burning and radiative terms Q_b and Q_R (blue dashed-dotted line).

D. Validation of the Model

To validate model of case breach we use results of a ground firing tests, in which fault occurs in a closure holding a pressure sensor. The closure is a metal disk covered by insulator material. A small leak arises on a boundary of the disk at moment $t = t_0$. Subsequently a small hole will grow due to surface melting and burning of the metal under the action of the hot gas flowing from the combustion chamber. The results of the reconstruction of the experimentally determined area of the case breach fault are shown in the Figure 9. At the input of the model we have time-traces of pressure and thrust, and known nominal parameters of the SRM and of the nozzle ablation. At the output we obtain the value of the fault area determined by forward integration of the model taking into account different mechanisms of the

heat conduction in the metal case. It can be seen from the figure that the physics model of the case breach fault can accurately reproduce the experimentally determined time traces of the fault and that the main contribution to the heat flow to the hole walls is given by radiation and burning. The analysis also allows one to determine the front velocity of the burning walls, which was found to be equal to $v_f = 0.27$ in/s. We now apply obtained results to the diagnostics and prognostics of the case breach fault in a large segmented SRM.

E. FD&P for the Case Breach Fault

To infer fault parameters the following quasi-stationary solution[29-33] for the nozzle stagnation pressure p_{ns} is used

$$p_{ns} = p_c \left[\frac{\Gamma c_0 \rho_p r_c}{\gamma p_c} \left(\frac{A_b(t)}{A_t(t) + A_h(t)} \right) \right]^{\frac{1}{1-n}}, \tag{18}$$

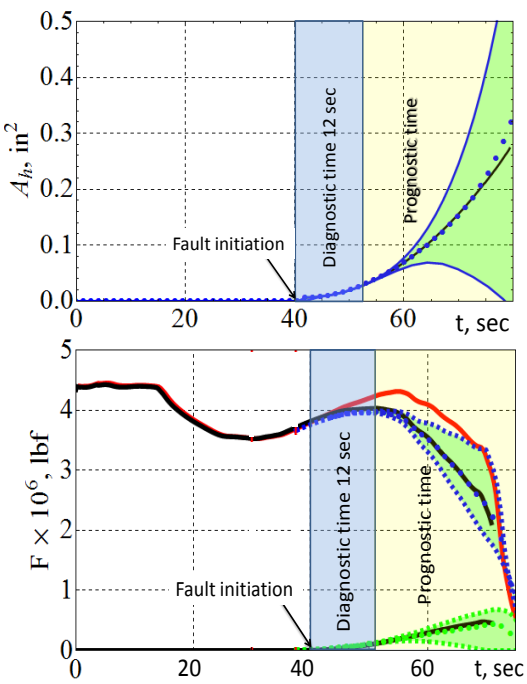

Figure 10 (top) Prognostic of the $A_h(t)$. The actual time series of the fault area $A_h(t)$ are shown by black lines. The mean values of predicted dynamics of the $A_h(t)$ are shown by blue dotted lines. The green shading indicates standard deviation of the predictions. The blue shading indicates the time used for diagnostic. The yellow shaded region indicates the prediction time. (bottom) The thrust in the nominal regime is shown by solid red line. The actual fault-induced time-traces of thrust and side load are shown by black lines. The time-traces of mean predicted values of the thrust and side load are shown by blue dots. The green shading indicates standard deviations for the predicted values. In the figures the prediction is made after ΔT_m=12 sec (right). Fault initial time T_f = 40 sec in all cases. The growth rate of the hole radius 0.3 in/sec.

Notice1[-31] that burning area $A_b(R(t))$ and nozzle throat area $A_t(t)$ are determined by measured nozzle stagnation gas pressure p_{ns}. The accuracy of the relation (18) is further improved by introducing the effective burning area $A_{be}(R(t))$ in the nominal regime. Indeed, in the nominal regime $A_h(t) = 0$ while $p_{ns}(t)$ and $A_t(t)$ are well known that allows us to determine uniquely the effective burning area $A_{be}(R(t))$ as a function of the burn distance $R(t)$. This functional dependence is assumed to be valid in the off-nominal regime of the case breach. Therefore, one can use data of the pressure sensor at the rocket head to estimate the deviations of the nozzle stagnation pressure p_{ns} from the nominal regime and subsequently to use equation (18) to estimate the area of the case breach fault $A_h(t)$ according to the following algorithm:

1) Use the nominal regime time-traces to determine the effective burning area by Eq. (18)
2) Use measured time-trace of the head pressure in the off-nominal regime $p_H(t)$ to find fault-induced pressure at the aft end using the fact that the pressure changes induced by the fault are uniform along the motor axis

$$p_A^{(fault)}(t) = p_A^{(nom)}(t) + \left(p_H^{(fault)}(t) - p_H^{(nom)}(t) \right);$$

3) Use nominal time-trace of the Mach number at the aft end to determined nozzle stagnation pressure

$$p_{ns}^{(fault)}(t) = p_A^{(fault)}(t) \left(1 - \frac{\gamma - 1}{2} M_{A,0}^2(t) \right)^{-1};$$

4) Determine time-trace of the hole area

$$A_h(t) = \left[\frac{\Gamma c_0 \rho_p a A_{b,eff}(t)}{\gamma \left(p_{ns}^{(fault)}(t) \right)^{1-n}} \right] - A_t(t) \cdot$$

The parameters of the fault dynamics $\{a_1, a_2, a_3, a_4\}$ are reconstructed from the inferred time-series data $A_h(t)$ using the least square method. We can now use the values of the parameters $\{a_i\}$ reconstructed during the diagnostic to predict fault and internal ballistics of the SRM forward in time.

Note that the values of the reconstructed parameters a_i and , therefore, the convergence of the forward predictions depend on the diagnostics time, which is one of the key characteristics of the FD&P system. The convergence of the predicted hole area time-traces towards actual time-traces of $A_h(t)$ is illustrated in Figure 10. In this test the hole area measurements are assumed to have sampling rate 1kHz and measurement noise 0.1%. The filtering procedure is used to reduce the noise in the data. The time interval ΔT_m used to infer fault parameters is 12 sec. The predictions are made up to 80 sec of the flight. Initially the $A_h(t)$ is reconstructed with the diagnostic time window ΔT_m=12 sec shown shaded by blue color, and the fault parameters $\{a_i\}$ are inferred. The dynamics of the fault is predicted ahead in time using inferred parameter values. Note that the convergence of the predictions of the hole area is achieved approximately after 11 sec of diagnostics.

F. Calculations of the Flight Safety Envelope

Let us consider now one of many possible applications of the developed model of case breach fault in large segmented SRMs. Objective of this application is to study response of the TVC of a large segmented motor to side thrust torque and compute at which moment the vehicle will leave the flight safety window. We introduce the flight safety window in the following way: altitude difference between the flight with the side thrust and the nominal flight is not larger than 4000 ft; the vehicle's angle of attack for the flight with the side thrust is in +20/-20 degrees interval. We assume that the flight is not safe if the rocket has altitude difference larger than altitude difference margin (4000 ft) or if the angle of attack of the rocket is larger than 20 degrees in abs value. We assume that the side thrust appears at forward and aft field joints at 0, 90, 180 and 270 degrees angle location at times from 0 to 120 seconds with 5 second interval. We use the model (34) to calculate nozzle and side thrusts, and the gas flow rate in the combustion chamber. The results of these calculations were fed into special purpose software to calculate rocket trajectory taking into account TVC. The simulations were performed about 200 times for different breach locations and different times. The envelope was created by plotting the side thrust profiles against the onset time of each fault for a given joint position and angle. The region of failure was then determined by plotting points of failure for each trajectory. These points were then extrapolated back in time in order to formulate the region of failure for the entire set of possible trajectories. It was found that for 0, 180 degrees breach location the rocket loses control due to rapid change of the altitude, for 90, 270 degrees breach location the rocket loses control mostly due to oscillations of the angle of attack. Some of the resulting flight envelopes are shown in Figure 11. The red colored regions indicate the mission loss due to the TVC failure caused by case breach fault.

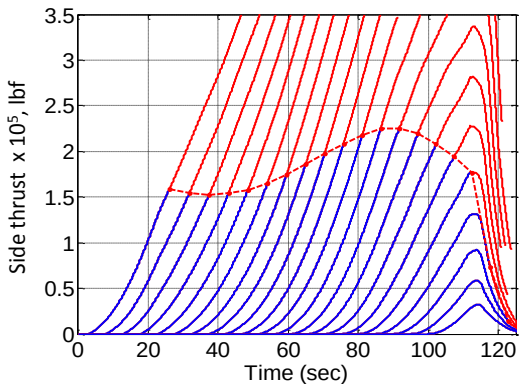

Figure 11. Side thrust values for 5th joint , 90 deg breach location. X-axis is start time of the side thrust. The hole radius growth rate was 0.3 in/sec.

V. Physics based modeling for Composite materials

As it was discussed in the previous sections the breach of the structural integrity was one of the key ingredients of the Challenger accident. In general structural faults may have multiple origin (including e.g. maneuvering loads, overpressure, external impacts etc.) and they may often lead to a catastrophic event. That is why on-board structural Health Monitoring (SHM) is one of the key NASA milestones on the way to safer space exploration. This is especially true for structures made from composite materials, which have been steadily replacing traditional structural components of space vehicles due to their high stiffness to weight ratios, stability under compressive forces, improved fatigue life, and good thermal and acoustic isolation properties.

However, many structural materials and especially composite materials have one basic handicap in common. They all have failure mechanisms that occur internally, out of view of normal visual means of inspection. Specifically, composite materials may suffer internal de-bonds, de-laminations, and cracks that are difficult and

expensive to detect using normal non-destructive inspection technique. For heavily loaded composites that will be employed by the next generation of the space vehicles, this type damage presents a major safety concern.

The development of the on-board SHM and associated FD&P system that will help to prevent accidents and mitigate their possibility catastrophic consequences in the future requires deep insight into physicist of failure combined with advancements in the signal processing. To illustrate this point we consider an example SHM method based on monitoring of elastic surface wave propagation in the composite structures, such as pitch catch and pulsed echo guided wave propagation and determination signature of scattering from the faults. This method requires a combination of mathematical modeling of the damaged composite structure, understanding of damage formation and behavior under external loads, and a good knowledge of the material properties and their effects on wave propagation characteristics[33].

A. Experiment

In order to gain insight into the SHM physics and evaluate SHM methodologies based on acoustic wave propagation an experiment was performed in collaboration with Metis Design Corporation (MDC) on a honeycomb-sandwich square panel 1ft x ft. The panel consists of two 84-mil thick cross-ply carbon fiber composite laminates (bonded to a 1 in-thick aluminum honeycomb core. The experimental setup used for SHM benchmarking SHM sensors is shown in Figure 12 (a). A schematic diagram of the panel with PZT sensor patch locations and numbering scheme are shown in Figure 12 (b). A PC-automated setup with two oscilloscopes (Tektronix TDS3014) and a function generator (Agilent 33220A) was used for data acquisition and signal generation. The data files from the PZT sensor patch were saved and then used for processing. The location of the sensors nodes can be seen from the plot and can be easily calculated (we considered that panel is centered at x=0,y=0). The panel was subject to controlled impacts of increasing energy. Diverse impact energies (10, 20, 30, 60 and 120 inch-lbs) were obtained by adjusting the dropping height in low-velocity impact tests to obtain a controlled damage at the center of the plate (coordinates (0,0)). The diameter of the semi-spherical impactor head is 1/2in. These impact energy levels were chosen based on the earlier calibration tests using another honeycomb panel to introduce hidden delaminations at the lower energy levels, a barely visible damage at intermediate levels, all the way up to visible damage at the higher energy levels.

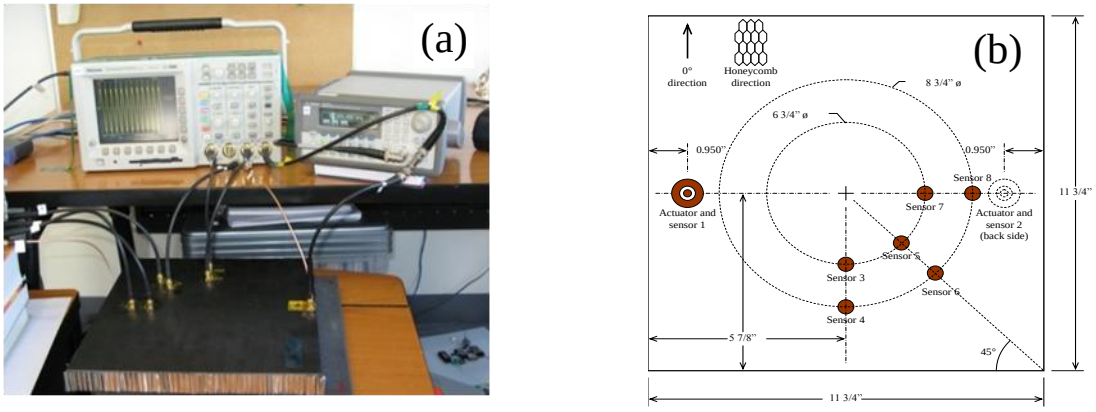

Figure 12 Photographs of experimental setup. (a) Panel with cabling and instruments; (b) A schematic diagram of the panel with PZT sensor patch locations and numbering scheme.

Lamb wave tests were done over a frequency range from 20 to 100 kHz. The data was collected at 10kHz intervals from 20 to 100 kHz. At each frequency, a 3.5-cycle Hanning windowed toneburst was used as an actuation signal. The actuator was excited for these tests and the responses on all sensors S1 through S8 were recorded. In addition, for the baseline and after the final impact, actuator A2 (located on the back side of the panel) was also excited to examine the possibility of detecting damage on one facesheet using PZT sensor patches on the opposite facesheet. Baseline data was collected, following which the panel was impacted multiple times with a calibrated impactor and the test data was collected after each impact.

B. Finite Element Model

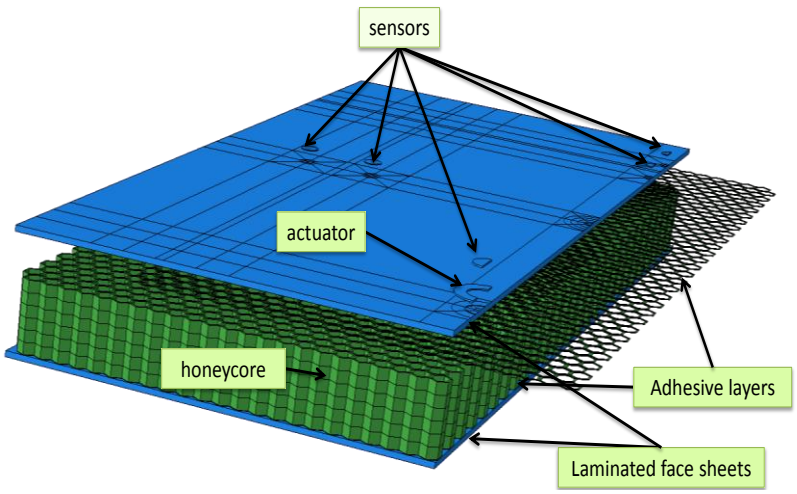

Figure 13 Finite element model . FE parts of the sandwich honeycomb structure with a piezoelectric actuator

Futher insight into the phenomena underlying physics of debonding, acoustic wave propagation, and scattering can be gained by binding a Finite Element modeling and theretical investifation and comparing these results with real experiment datafor Pitch-Catch and Pulse-Echo signals obtained from coresponding PZT sensors. The details of the finite element model built in Abaqus to simulate wave propagation can be found somewhere esle[35-38]. It should be mensioned that in this model we have taken into account all charactersitic features of real honeycomb panel: CFRP facesheets and a softhonycomb core between them. In addition to these components, we develop an adhesive layer model binding facesheets with the core. The thickness of the adhesive layer considered equalt the thikness of one ply in 14th layered laminate plate. We also consider PZT actuator and sensors mounted on the panel (see Figure 13). As a result of simulation, electrical signals of the sensors were compared with the signals obtained experimentally. Such approach best fits the typical sketch we have in SHM when measured signals are used for interpretation of changes in monitored panels. The developed model was also used to simulate the calibrated impact of the panel and to investigated scattering of the surface waves in the impacted panel. The developed model contain a milions of nodes and requures a few hours of simulation on i7 8-core desktop.

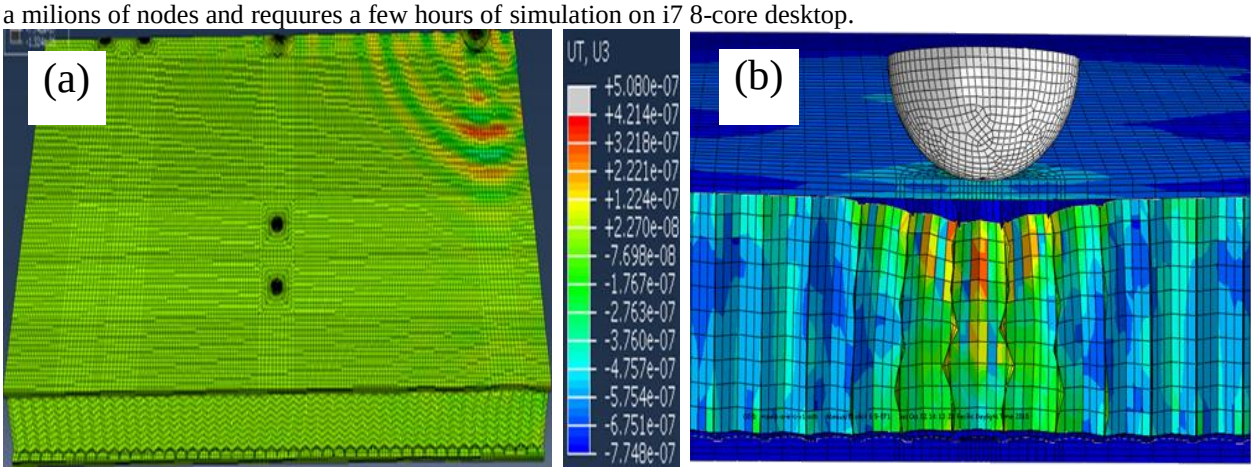

Figure 14. (a) Out–of-plane displacement for t=0.06ms (PZT sensors corresponding experimental layup are denoted black circles); (b) Results of the simulations of the impact showing crashed honeycomb core.

The typical approach of this study is to model wave propagation field in 3D sandwich honeycomb panel and to fit these results to SHM experimental data. First, propagation of the acoustic waves excited by annular PZT patch was simulated without damage (see Fig. 14 (a)). Next, we simulate the calibrated impact and investigate the crash of the honeycomb core and debond of the facesheet. Finally, scaterred by the debond (damaged area) signal was collected as a voltage from the top surface of the sensors in the FE model and compared with an electrical signal in pitch catch and pulse-echo technique. In the experiment and numerical simulations a narrowband 3.5-cycle Hanning-windowed waveform is applied to the actuator PZT generating Lamb waves. The simulations show a very good agreement of both the theoretical and experimental data at the initial stage of wave propagation.

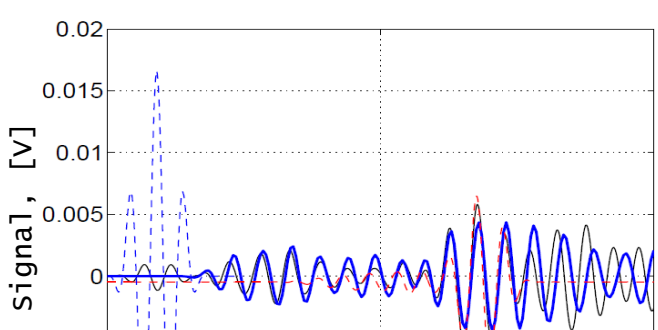

The wave modes reflected off from the boundaries of the plate are out of phase

cs and Astronautics

with the experimentally measured signal. An example of the results of the simulations of the wave propagation in honeycomb structure are shown in Figure 15 in comparison with the experimental results measured for 100 kHz on sensor # 4. The blue line corresponds to FE modeling, black one to experimental results and dashed red line to the modes calculated by Mindlin plate theory approach. One can see that for the longer time there is a discrepancy between the simulated and experimental signals even for the pristine panel without damage. This is probably due to imperfections in the panel manufacturing and nonperfect boundary conditions in experiment in contrast to perfect geometry we use in numerical simulation. Note that although high fidelity simulations provide a convenient tool for validation and verification of the model they cannot be employed for onboard SHM and further analytical and physical insight is required for reliable and timely detection of the structural faults.

C. Analytical investigation of resonance scattering

Moreover, deep physical insight into the scattering phenomena may reveal new features in the scattered signals, which in turn can be used to develop more reliable SHM methods. In this section we illustrate such an approach using as an example analysis of the resonance scattering from the fault. In this case mathematical model of the fault is crucial. In framework of this approach a Mindlin plate theory will be used where the sate of the plate is described by three Helmholtz equations[39]

$$\Delta W_i + k_i^2 W_i = 0,\ i=1,2,3 \qquad (19)$$

where W_i system variables and Δ - Laplace operators. The dispersion curves for a typical sandwich panel corresponding to three branches $k_i(\omega)$. The flexural wave corresponds to the real $k(\omega)$. The second (and third) dilatation branch of $k(\omega)$ dependence become real starting from the cutoff frequency.

We introduced a model of the fault describing debond (delamination) sketch of which is presented in Figure 16. This fault is developed as a small size circular region (index 3, Figure 16) attached by its boundary to the same size circular domain (index 2). Both domains (2 and 3) are connected with the rest of the panel (index 1) via properly chosen boundary conditions. The equations of motion (19) are solved with corresponding set of parameters for each domain: for the healthy panel denoted with index 1 and for the delaminated region denoted by indices j=2,3. Therefore for each domain (j = 1,2,3) we have three dispersion relations (i = 1,2,3) k_{ij}. As a result, we get a square matrix of k_{ij} where the first index is a number of a root in the dispersion relation and the second number denotes the media (j=1,2,3). For example, k_{1j} where 1 denotes the first root is calculated for j=1 for $r > a$ and for j=2,3 for $r < a$. To be specific we consider propagation of a signal corresponding to the two modes k_{11} and k_{21}. This wave is scattered by the debond region described by the boundary condition. These conditions include the continuity of the plate displacements, the equality of the slopes and moments at $r=a$ as well as equality of the moments and shear forces across the fault boundaries.

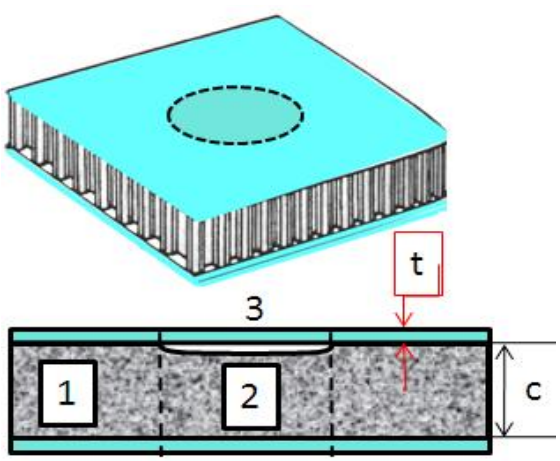

Figure 16. Model of the debond (delamination) fault.

The solution of the system will contain two important terms: incident wave w^{in} generated by PZT sensor and scattered one vanishing at the infinity. This solution can be expended in Fourier series in polar angle θ and for the domains j=1,2,3 is presented by

$$W = \sum_{n=0}^{\infty} \cos(n\theta) \begin{cases} w^1 \equiv w_n^{in} + a_{1n} H_n(k_{11} r) + a_{2n} H_n(k_{21} r)\,|_{r>a} \\ w^3 \equiv a'_{5n} J_n(k_{13} r) + a'_{5n} J_n(k_{23} r)\,|_{r\le a} \\ w^2 \equiv a_{4n} J_n(k_{12} r) + a_{5n} J_n(k_{22} r)\,|_{r\le a}; \end{cases} \qquad (20)$$

where J_n and H_n are the Bessel and the Hankel functions of the first kind, respectively. In what follows let us consider the case of sufficiently high frequency f of the source: $\omega=2\pi f > \omega_c$, where ω_c is the cutoff frequency. For the elastic field around the circular debond the

scattering coefficients $a_{1n,}$ and a_{2n} determine displacements outside the debond region. To find the scattering coefficients $a_{1n,}$ and a_{2n} a system of linear algebraic equations

$$A_n \mathrm{u}_n = b_n \tag{21}$$

has to be solved for each value of n.

As a result we obtain a system of linear algebraic equations relative to constants

$$u_n = (a_{1n}, a_{2n}, a_{3n}, a_{4n}, a'_{4n}, a_{5n}, a'_{5n}, a_{6n}, a'_{6n})^T,$$

which can be solved

$$a_{1n}(\omega) = \frac{\det A_{1n}(k_{ij}(\omega)a)}{\det A_n(k_{ij}(\omega)a)}, \qquad a_{2n}(\omega) = \frac{\det A_{2n}(k_{ij}(\omega)a)}{\det A_n(k_{ij}(\omega)a)}. \tag{22}$$

The matrix A_n and vector b_n and complete set of the matrix elements can be obtained by using symbolic calculus and for simplicity is omitted here. In expressions (22) matrix $A_{1n}(k_{11}a)$ is obtained by substituting the first column in matrix $A_n(k_{11}a)$ by the left hand side column, and matrix $A_{2n}(k_{12}a)$ - by substituting the second column by the right hand side column. As a result, for out of plane displacement for $r>a$, the formula can be presented as

$$w(r,\theta,\omega) = \mathrm{Re}\sum_{n=0}^{\infty}\cos(n\theta)[w_n^{in}(r) + a_{1n}(\omega)H_n(k_{11}(\omega)r) + a_{2n}(\omega)H_n(k_{21}(\omega)r)]e^{-i\omega t} \tag{23}$$

It can be seen from the analysis of the expressions for $a_{1n,}$and a_{2n} that the shape of the scattered signal depends on a large number of structural and geometric parameters. Let us consider in more details how amplitudes of the scattered signal depend on the frequency, debond thickness, and the size of the fault, while all other parameters are fixed. It should be noted that for small values of the debond radius a ($a < 1cm$) the Mindlin plate theory is not valid for sandwich parameters under consideration, therefore our analysis is restricted by the minimum size of the fault about 1cm. Consider as an example the magnitudes and phases of the coefficients a_{10} and a_{11} for the debond ($t_d = t_f$) and delamination faults ($t_d < t_f$) for breathing (n=0) and dipole (n=1) modes in the series presented in Eq. (23). The results of the corresponding calculations are shown in Figure 17. It can be seen from the figure that these phases

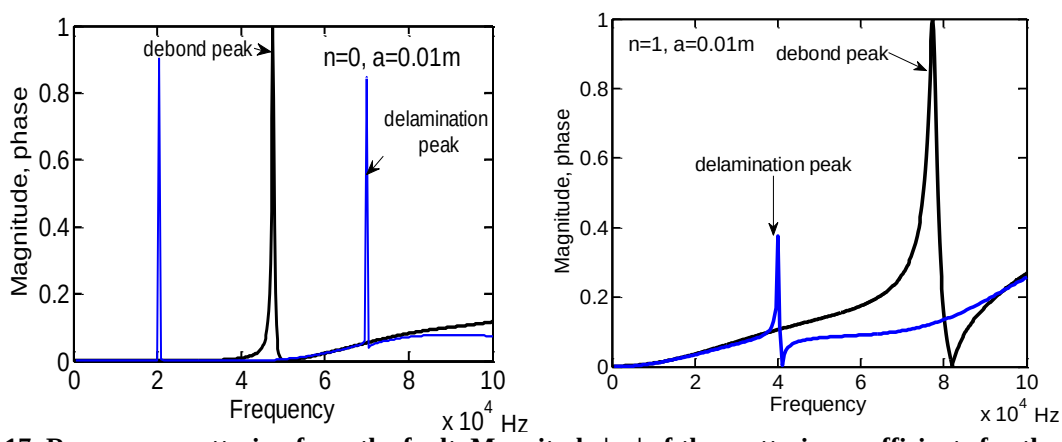

Figure 17. Resonance scattering from the fault. Magnitude $|a_{1j}|$ of the scattering coefficients for the fault of size a = 0.01m versus the frequency $f = \omega/2\pi$ for the first two modes: breathing mode – (a) and dipole one – (b). Magnitudes for the debond fault are depicted by a black solid line, and for the same size delamination (t_d = 0.25ft) – by a blue line.

experience a shift equal to π by passing through the resonance frequency. It can also be seen from the figure that for a sufficiently small fault (size of the fault is comparable with the thickness of the plate) we have one resonance peak for each mode for a considered frequency range (<100kHz) of the debond fault and that the number of peaks increases as the resonance frequency decreases for the delamination mode (Figure 17). The first eigenfrequency of the debond has a much higher frequency than for the delamination fault of the same size. In this case one can observe more peaks belonging to a delamination than to a debond in the frequency range f < 100kHz. The thinner is the debond (small $t_d < t_f$) the lower is a distance between eigenfrequncies of the fault in the fault spectrum. These analytical findings were further verified using results of the high-fidelity simulations.

The observed features of the guided wave propagation and scattering in sandwich structures can be used to develop more accurate and reliable SHM. Indeed, the number, the size, and the width of the resonances can be now related directly to the size and severity of the fault and to the damping of the structural fault. Such interrelations can be conveniently integrated into the onboard SHM using advanced Bayesian techniques of parameter estimation developed in our earlier work[33,37,40].

VI. Conclusion

In this paper we consider operational physics analysis of a number of critical engineering problems that were identified from the analysis of Challenger accident. It was shown that corresponding problems appear at the interface of the seemingly distant engineering and physics domains and their analysis requires in particular deep understanding of ignition and explosion in cryogenic mixtures, internal ballistics of SRM's in nominal and off-nominal regimes, structural health and integrity of space vehicles. It was also shown that there exists a deep interrelation between the physics-based approaches to the analysis of critical engineering problems and Integrated System Health Management required for the safer space exploration in the future. The existence of such interrelation was illustrated in discussion of the recent progress in the development of the leading-order physics models that capture main casual relations and allow for sensitivity studies and Engineering Risk Assessment for onboard SHM and FD&P for SRMs.

In particular, we have proposed a cavitation-induced mechanism of self-ignition of cryogenic hydrogen/oxygen mixture. Self-ignition is caused by injection of the hot gas and the strong shock waves generated by the cavitation collapse of oxygen vapor bubbles near the surface of the oxygen liquid and explosive H2Ox mixture. Our approach based on cavitation-induced ignition and aerosol combustion of cryogenic hydrogen/oxygen mixture have described characteristics of explosion waves in different HOVI tests and have shown that depending of the geometry of the rupture devices used in HOVI tests the type of explosion wave can vary from slow deflagration to supersonic combustion and even to strong detonation explosion. Our analysis has showed that only a small fraction of the escaped cryogen mass participates in formation of the strong explosion waves.

Next the results of the work in progress on the development of hybrid probabilistic algorithms for SRMs on-board ISHM system were presented. We introduce model that describe accurately internal ballistic of SRM in nominal and off-nominal regime. The model is verified by comparison with the results of high-fidelity simulations. A number of algorithms are derived to infer fault parameters and to predict fault dynamics. The algorithms accommodate abrupt changes in the model parameters and can be used to develop hybrid probabilistic on-board SRM ISHM. The performance of the algorithms was tested using analysis of the experimental time-series data. It is shown that the algorithm can be successfully applied for the prognostics of the case breach fault. The model is used to develop on-board FD&P of the case breach fault and applied to predict fault-induced internal ballistics of a large segmented SRM. The developed methods and algorithms can be used to analyze other SRM' faults, including overpressure and breakage of the case induced by nozzle blocking, bore choking and grain deformation. In all these cases the fault dynamics is governed by the changes in the burning area and/or effective nozzle area. Therefore the model introduced in this work can be efficiently applied to analyze of these faults and develop on-board FD&P.

In our final example a problem of onboard structural health monitoring of critical structural components of the next generation heavy lift vehicle was considered. It was shown that physics based analytical modeling of the ware propagation and scattering in sandwich composite plates combined with a high-fidelity modeling validated by comparison with experimental data allows one to develop new more reliable and accurate SHM methods. In particular, the analytical investigation of the plate wave using the Mindlin plate theory and the numerical simulations reveals the existence of characteristic resonant features in the scattered signals. This insight shows how these features including the number, the size, and the width of the resonances can be related directly to the size and severity of the fault and to the damping of the structural fault.

Considered examples emphasize one important point. The complexity and high level of integration of modern engineering systems and challenges these systems possess for the Engineering Risk Assessment demonstrate a significant and growing need in a unified approach to an analysis of critical engineering systems in complex operational-mission environments. Such an approach can be conveniently developed within emerging discipline – operational physics of critical engineering missions. It will help in technology definition process by reducing risks of selecting among the competing technologies, by providing guidance in the development of these technologies, integration of different technologies into a complete system and choice of cross-cutting, flexible developmental paths combined with the Integrated System Health Management.

Acknowledgments

References

[1] Cole, M.D., "*Challenger: America's space tragedy*", Springfield, N.J., Enslow Publishers, 1995.

[2] Vaughn, D., Diane, V., "*The Challenger Launch Decision: Risky Culture, Technology, and Deviance at NASA*", University of Chicago Press, Chicago, 1996.

[3] Osipov, V., Muratov, C., Hafiychuk, H., Ponizovskya-Devine, E, Smelyanskiy, V., Mathias, D., Lawrence, S., Werkheiser, M., "Hazards Induced by Breach of Liquid Rocket Fuel Tanks: Conditions and Risks of Cryogenic Liquid Hydrogen-Oxygen Mixture Explosions", NASA Report ARC-E-DAA-TN2747, 2011.

[4] Brennen, C. E., "*Fundamentals of Multiphase Flow*", Cambridge University Press, 2005; Brennen, C. E., "*Cavitation and Bubble Dynamics*", Oxford University Press, 1995.

[5] Fujikawa S. and Akamatsu, T., "Effects of the non-equilibrium condensation of vapor on the pressure wave produced by the collapse of the bubble in a liquid", *J.Fluid Mech.*, Vol.97, part 3,1980, pp.481-512.

[6] Clark, J. A.,"Universal Equations for Saturation Vapor Pressure", *40th AIAA/ASME/SAE/ASEE Joint Propulsion Conference and Exhibit*, Fort Lauderdale, Florida, July, 2004.

[7] Osipov, V. V., Muratov, C. B. Ponizovskaya-Devine, E, Foygel, M, Smelyanskiy, V. N., "Cavitation-induced ignition mechanisms in cryogenic hydrogen/oxygen mixtures" , *Appl. Phys. Lett.*, Vol.98, 134102, 2011.

[8] Glassman, I. and Yetter, R. A., "*Combustion*", 4th edition, Elsevier, New York, 2008.

[9] Williams, F. A., "*Combustion Theory*", Addison-Wesley Publishing Company, Inc., Princeton University, 1985.

[10] Kao S, Shepherd J. E, "Numerical solution methods for control volume explosions and ZND detonation structure", GALCIT Report FM2006.007 (CANTERA- http://www.galcit.caltech.edu/EDL/).

[11] Michael, J.V., Sutherland, J.W., Harding, L.B., Wagner, A.F., "Initiation in H2/O2: rate constants for H2+O2 →H+HO2 at high temperature", *Proceedings of the Combustion Institute*, 28, 1471-1478,2000.

[12] Mitani, T. and Williams, F. A. Studies of Cellular Flames in Hydrogen–Oxygen–Nitrogen Mixtures, Combustion *and Flame*, Vol. 39, 1980, pp. 169–190.

[13] Landau, L. D., Lifshitz, E. M., "*Course of Theoretical Physics*", Vol. 6, Butterworth-Heinemann. Oxford, 1987.

[14] Plaster, M., McClenagan, R.D., Benz, F.J., Shepherd, J.E., Lee, J.H.S., "Detonation of Cryogenic Gaseous Hydrogen-Oxygen Mixtures", *Prog. Astronaut. Aeronaut.*, v.133, 1991, pp.37-55.

[15] Groethe, M., Merilo, E., Colton, J., Chiba, S., Sato, Y., Iwabuchi, H., "Large-scale hydrogen deflagration and detonation", *International Journal of Hydrogen Energy* v.32, 2007, pp. 2125 – 2133.

[16] Merilo, E.G., Groethe, M.A., "Deflagration Safety Study of Mixtures of Hydrogen and Natural Gas in a Semi-open Space", *In Proceedings of the international conference on hydrogen safety*, S. Sebastian, Spain, 2007.

[17] Jouot, F., Dupre, G., Quilgars, A., Go¨kalp, I., Cliquet, E., "Experimental study of detonation in a cryogenic two-phase H2–O2 flow", *Proceedings of the Combustion Institute* , Vol.33, 2011, pp.2235–2241 .

[18] Nikolaev, Yu. A. , Vasil'ev, A. A. and Ul'yanitskii, B. Yu. , "Gas Detonation and its Application in Engineering and Technologies (Review)", *Combustion, Explosion, and Shock Waves*, Vol.39, 2003, pp.382–410.

[19] Short, M., "The initiation of detonation from general non-uniformly distributed initial conditions", *Philosophical transactions*, Vol.353, 1995, pp.173-203.

[20] Kapila, A. K., Schwendeman, D. W., Quirk, J. J., Hawa, T., "Mechanisms of detonation formation due to a temperature gradient", Combustion *Theory and Modeling*, Vol.6, 2002, pp. 553-594.

[21] Molkov, V., Makarov D. and Schneider, H., "LES modeling of an unconfined large-scale hydrogen–air deflagration", *J. Phys. D: Appl. Phys.*, Vol.39, 2006, pp. 4366-4376; "Hydrogen-air deflagration in open atmosphere: Large eddy simulation analysis of experimental data", International *Journal of Hydrogen Energy*, Vol.32, 2007, pp. 2198-2205.

[22] Lei Xu, Wendy W. Zhang, and Sidney R. Nagel, "Drop Splashing on a Dry Smooth Surface", *Phys. Rev. Lett.* Vol.94, 184505, 2005.

[23] Ahmed, M., Ashgriz, N. and Tran, H. N., "Influence of Breakup Regimes on the Droplet Size Produced by Splash-Plate Nozzles", *AIAA Journal*, Vol. 47, No. 3, 2009, pp. 516-522.

[24] E.J. Allin, W.F.J. Hare and R. E. MacDonald, "Infrared absorption of liquid and solid hydrogen*", Phys. Rev.,* Vol. 98, 1955, pp. 554-555 .

[25] E.J. Allin, H.P. Gush, W.F.J. Hare and H.L. Welsh, "The infrared spectrum of liquid and solid hydrogen", *Il Nuovo Cimento*, Vol.9, Supplement 1 1958,pp. 77-83.

[26] Report of the Presidential Commission on the Space Shuttle Challenger Accident, DIANE Publishing, 1986, (/ http://history.nasa.gov/rogersrep/genindex.htm).

[27] Sailta, M., "Verification of Spatial and Temporal Pressure Distribution in Segmented Solid Rocket Motors," *Proceeding of AIAA paper 89-0298, 27th Aerospace Science Meeting*, Reno, Nevada, 1989, January.

[28] Culick, F. E. C. & Yang, V.. *Prediction of the Stability of Unsteady Motions in Solid Propellant Rocket Motors, Nonsteady Burning and Combustion Stability of Solid Propellants*, edited by L. De Luca, 1992; E. W. Price, and M. Summerfield,, Progress in Astronautics and Aeronautics, *AIAA*, Washington, DC, Vol.143, pp. 719–779.

[29] Luchinsky, D.G. ; Osipov, V.V. ; Smelyanskiy, V.N. ; Timucin, D.A. & Uckun, D. S., "Model based IVHM system for the solid rocket booster " , *Proceeding of Aerospace Conference, 2008 IEEE*, 1-8, March, BigSky, Montana, 2008, pp.1 – 15.

[30] Osipov, V. V. ; Luchinsky, D. G. ; Smelyanskiy, V.N. ; Lee, S. ; Kiris, C. & D. Timucin. (2007, March), "Bayesian Framework for In-Flight SRM Data Management and Decision Support", in Proceeding of IEEE 2007 Aerospace Conference, Big Sky.

[31] Luchinsky, D.G. ; V.V. Osipov, V.N. Smelyanskiy, D.A. Timucin, S. Uckun, B. Hayashida, M. Watson, J. McMillin, D. Shook, M. Johnson, S. Hyde. (2009), "Fault Diagnostics and Prognostics for Large Segmented SRMs", in Proceeding of 2009 IEEE Aerospace Conference, Big Sky, March, Montana.

[32] D.G. Luchinsky, V.V. Osipov, V.N. Smelyanskiy, I. Kulikov, A. Patterson-Hein, B. Hayashida, M. Watson, D. Shook, M. Johnson, S. Hyde, J. Shipley, Integrated Vehicle Health Management for Solid Rocket Motors, INTECH, Croatia, 2010.McMillin, J.E. (2006, July). AIAA 2006-5121, in Proceeding of 42nd AIAA/ASME/ SAE/ASEE Joint Propulsion Conference & Exhibit , Sacramento, CA.

[33] D.G. Luchinsky, V.V. Osipov, V.N. Smelyanskiy, I. Kulikov, A. Patterson-Hein, B. Hayashida, M. Watson, D. Shook, M. Johnson, S. Hyde, J. Shipley, Integrated Vehicle Health Management for Solid Rocket Motors, INTECH, Croatia, 2010.

[34] Mindlin R. D., and Deresiewicz H. 1954. Thickness-shear and flexural vibrations of a circular disk. Journal of applied physics. Vol. 25. #10, 1328-1332.

[35] V. Smelyanski, V. Hafiychuk, D.G. Luchinsky, C.Banks, J.Miller, M.Watson, "Theoretical Background and Prognostic Modeling for Benchmarking SHM Sensors for Composite Structures", Annual Conference of the Prognostics and Health Management Society 2010, http:// www.phmsociety.org/vents/conference/phm/10/proceedings

[36] D.G. Luchinsky, V. Hafiychuk, V. Smelyanskiy, R.W. Tyson, J.L. Walker, J.L. Miller, "High-fidelity modeling for health monitoring in honeycomb sandwich structures", Aerospace Conference, 2011 IEEE, DOI: 10.1109/AERO.2011.5747569, Publication Year: 2011 , Page(s): 1 - 7.

[37] V. N. Smelyanskiy, D. G. Luchinsky, V. Hafiychuk, V. V. Osipov, I. Kulikov, A. Patterson-Hine, "Physics-Based Methods of Failure Analysis and Diagnostics in Human Space Flight", book chapter in "Machine Learning and Knowledge Discovery for Engineering Systems Health Management" by A. N. Srivastava, J. Han (Edts), Taylor & Francis, New York, 2011.

[38] Luchinsky, D. G., Hafiychuk, V., Smelyanskiy, V., Tyson, R. W., Walker, J. L., Miller, J. L. 2011. High-Fidelity Modeling for Health Monitoring in Honeycomb Sandwich Structures. Report Number: ARC-E-DAA-TN3100.

[39] Mindlin R. D., and Deresiewicz H. 1954. Thickness-shear and flexural vibrations of a circular disk. Journal of applied physics. Vol. 25. #10, 1328-1332.

[40] Smelyanskiy, V. N., D. G. Luchinsky, D. A. Timuçin, and A. Bandrivskyy. (2005a), "Reconstruction of stochastic nonlinear dynamical models from trajectory measurements", Phys.l Rev. E, Vol. 72, 026202.